The Semiconductor Field-Emission Photocathode

DIETER K. SCHRODER, MEMBER, IEEE, R. NOEL THOMAS, JAMES VINE, AND H. C. NATHANSON, MEMBER, IEEE

***Abstract*—The recently developed large-area field-emission photocathode is described. It consists of a finely spaced array of point emitters fabricated by etching of p-type silicon or other semiconductor. Uniform emission over areas of 6–7 cm² have been obtained. For Si, the spectral response extends from 0.4 to 1.1 μm. Quantum yields of 25 percent at 0.86 μm have been measured, which is about five times the value reported for the extended S-20 photocathode and comparable to the best III–V photoemitters. Calculations indicate that quantum yields of up to 40 percent at 0.86 μm and 28 percent at 0.9 μm are attainable with the present photocathode structures. For low dark current densities, photocathode cooling to temperatures approaching 77 K must be employed at present. The dark current is shown to be dominated by surface-generated electrons in the space-charge region of the emitters. Effects of phosphorus gettering and annealing treatments on dark current are discussed, and the spatial frequency response of the device is determined. The results of a computer study show that the field intensification factor of p-semiconductor field emitters behaves quite differently from that of metallic emitters.**

I. INTRODUCTION

ELECTRON emission into vacuum from semiconducting field emitters under the influence of an external electric field has been extensively investigated during the past few years. These studies were performed using single-field emitters and indicate clearly that field emission from p-type Si [1], Ge [2], and other semiconductors [3],[4] is strongly photosensitive. Photoelectric yields approaching and even exceeding unity have been reported for Si [5] and Ge [2],[5]. While single emitters are useful for investigative studies, they are hardly practical as field-emission photocathodes. However, an array of field emitters such that the electron current from each emitting tip is proportional to the light falling on it, presents a novel approach to photoemission, and such a device could be of considerable importance since photoemission using the field-emission effect does not have a long wavelength threshold as encountered in cesiated III–V photocathodes [6].

Attempts have been made in the past to develop photo field-emission arrays. Bibik *et al.* [7] have reported efficient photoemission from small-area (0.5 cm²) field emitters made of Si and Ge, and Arthur and Wagner employed the VLS epitaxial growth technique to form dense, needle-like emitters on flat silicon substrates [8]. We have recently succeeded in fabricating large-area arrays (up to 6–7 cm²) of p-type silicon field emitters [9]. They are photosensitive and emit electrons into vacuum with an exceptionally high degree of uniformity. Broadband photoemission has been observed with responsivities at visible and near infrared wavelengths comparable to those of the III–V negative-electron-affinity photoemitters. In the transmissive mode of operation, primary quantum efficiencies of 25 percent at 0.86 μm were measured. The high photoresponse is attributed to a high tunneling probability at the surface and long minority carrier diffusion lengths in the high-resistivity p-silicon. The field-emission photocathode is unique in that photoemission is observed without the use of cesium or cesium-oxide activation, unlike other types of photosurfaces. Consequently, high-processing temperatures and stringent high-vacuum conditions are not required, thus making the silicon-array field-emitter compatible with present-day image-tube fabrication methods.

In this paper, the principle and operating characteristics of the field-emitter photocathode are given. In Section II, the physics of photosensitive field emission from p-type semiconductors is described. The field-intensification factor, β, is analyzed in Section III by computer studies and it is shown that it behaves very differently from that of metallic emitters. β is high when the p-emitter operates in the Fowler–Nordheim region and drops when the operating point shifts into the saturation regime, thus establishing a self-ballasting feedback mechanism. The dark current is discussed in Section IV and is shown to be the result of thermal generation of electron-hole pairs in the depleted space-charge region at the emitting surface, dominated by surface generation. The effects of phosphorus gettering and annealing treatments showing the importance of surface states are treated in Section V. In Section VI, the spectral response and quantum yield are given, both experimentally and theoretically. It is shown that the field emitter photocathode is the only existing cathode with efficient photoresponse beyond 1.1-μm wavelength. Finally, in Section VII, the spatial frequency response is analyzed by considering both lateral minority carrier diffusion and the discrete nature of the device. It is shown that modulation transfer function values of 40 percent at 15–20 line pairs/mm are possible with existing devices. For optimized designs, 65 percent at 20 line pairs/mm and limiting resolutions of 80 line pairs/mm are predicted.

Manuscript received May 17, 1974; revised August 8, 1974. This work was supported in part by the Advanced Research Projects Agency and monitored by the Night Vision Laboratory, Fort Belvoir, Va., under Contract DAAK 02-72-C-0399.

The authors are with the Westinghouse Research Laboratories, Pittsburgh, Pa. 15235.

Authorized licensed use limited to: IEEE Xplore. Downloaded on March 6, 2009 at 10:39 from IEEE Xplore. Restrictions apply.

II. FIELD EMISSION FROM p-TYPE SEMICONDUCTORS

Field emission from metallic emitters is well described by the Fowler–Nordheim (F–N) theory [10] and the emission current is given by

$$I_e = 1.54 \times 10^{-6} \frac{E^2}{\phi} A_e \exp\left(-6.83 \times 10^7 \phi^{3/2} v(y)/E\right) \tag{1}$$

where E is the electric field, ϕ is the work function, A_e is the emitter area, and $v(y)$ is a slowly varying function [11] that represents the Schottky lowering of the potential barrier. The preexponential term is the supply function and the exponential term is the transmission coefficient. For $\phi \simeq 4$–5 eV, field emission is normally observed at $E \simeq 1$–5×10^7 V/cm. Plots of log (I_e/E^2) versus $1/E$ are linear. It is usually more convenient to plot log I_e versus $1/V_A$, which is also linear to a good approximation. In addition to metals, n-type semiconductors generally also yield linear F–N behavior [12], indicating that as for metallic emitters, the supply of electrons within the emitter is sufficient for the emission to be determined only by the transparency of the surface barrier.

Field emission from p-semiconductors is considerably more complex for several reasons. Emission can be strongly influenced by the state of the surface, field penetration into the semiconductor, limited availability of electrons, and by the fact that emission can arise from both conduction and valence bands. Deviations from a F–N dependence are usually observed for p-type emitters [1]. Theoretical treatments of field emission from semiconductors have been attempted [12] and numerical solutions do indeed depict certain deviations from F–N behavior, but in many important aspects, experimental observations are not adequately described by theoretical predictions.

The general features of field emission from p-type semiconductors have been discussed by others [13],[14] and are summarized in Fig. 1. The four important regimes of operation are shown by regions I–IV. In region I, there is a sufficient number of electrons in the conduction band, and the emission current is determined only by the tunneling probability at the surface. For the higher voltages in II, field penetration creates a depletion region and causes the current to be limited by the supply of electrons and not the transparency of the barrier. At the still higher voltages of region III, the field penetration is generally considered to be sufficiently strong that impact ionization in the space-charge region (scr) causes the rapid current increase shown. Since in both II and III the supply of electrons is limited, external excitation and temperature will cause the current to increase. With further increases in applied voltage (region IV), the rapidly increasing emission current will again become restricted by the surface-vacuum barrier transparency [15].

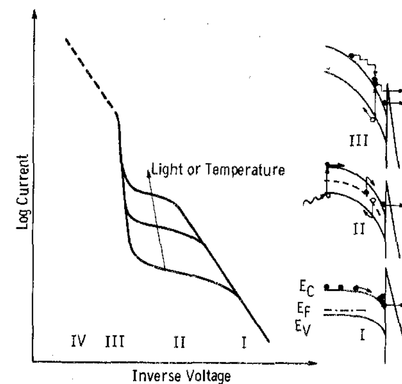

Fig. 1. Current–voltage characteristics of a p-type semiconductor field emitter showing the effects of light and temperature. The energy band diagrams correspond to regions I, II, and III.

Almost all experiments in the past have been performed with individual emitters, both for metals and semiconductors. When dealing with the simultaneous emission from a multiplicity of emitters where variations in emission from individual emitters may exist, the question arises as to whether F–N behavior (as in region I in the case of p-Si) is to be expected at all. This problem has been treated by Tomaschke and Alpert [16], who, by numerical methods, were able to show that groups of up to 100 emitters with randomly selected field enhancement factors and emitting areas do indeed yield linear F–N plots. Ample experimental confirmation of this result is provided by our data [17] which indicate conclusively that the simultaneous emission from almost a million emitters has a linear F–N dependence on voltage. It would therefore appear that analyses of individual emitters are appropriate to arrays of many such emitters.

III. FIELD INTENSIFICATION

The electric field, E, appearing in the F–N expression (1) is that at the tip of the field emitter. E can be written as

$$E = \beta E_V \tag{2}$$

with

$$E_V = V_V/d \tag{3}$$

where d is the anode-to-emitter spacing, V_V is the voltage applied between anode and emitter, and E_V is the field due to V_V if the emitter surface were planar. It has generally been assumed that β, the field intensification factor, depends only on the geometry of the emitter and is independent of the applied voltage. This is clearly justified for metallic emitters, where the log(current)–inverse voltage relationship is linear. Quite a different situation is found in p-type semiconductors, where the field can penetrate into the emitter and its surface is no longer an equipotential surface.

In order to determine the dependence of β on the geometry and the applied voltage, a detailed computer study was carried out. The results are presented in this section for both metallic and p-semiconductor field emitters. It is shown that while for a metallic emitter β is inversely

Authorized licensed use limited to: IEEE Xplore. Downloaded on March 6, 2009 at 10:30 from IEEE Xplore. Restrictions apply.

proportional to the tip radius, for a p-type semiconductor, it is much lower and quite insensitive to the radius, once a depleted scr develops. n-type semiconductor emitters behave like metals, provided the electron emission is governed by the barrier transparency and not the supply of electrons within the emitter [18].

The computer study was carried out to find an exact solution to the shape of the scr, the electric field distribution in and around the emitter and the field intensification factor, by using a relaxation method to solve the partial differential equations. Starting with an infinite array of identical emitters all under the same electrical conditions, each emitter may be regarded as being at the center of a rectangular cell, extending from the base plane of the silicon to the anode, as shown in Fig. 2(a). All the cells are identical and it is only necessary to solve the electrostatic field problem in any one of them, imposing the boundary condition of zero normal potential gradient on the cell faces that adjoin neighboring cells, i.e.,

$$\partial V/\partial n = 0. \tag{4}$$

To reduce the three-dimensional problem to one in two variables, the cell was approximated by a circular cross section of diameter S, imposing (4) on the cylindrical surface. The problem is then one of axial symmetry in coordinates r and z, as shown in Fig. 2(b).

The electrostatic potential obeys Laplace's equation

$$\nabla^2 V = 0 \tag{5}$$

in the vacuum. As a result of the carrier depletion, there exists a charge in the silicon where the potential is governed by Poisson's equation

$$\nabla^2 V = -\rho/K_s\epsilon_0. \tag{6}$$

The charge density ρ varies with voltage and was taken to be

$$\rho = \rho_0\left[1 - \exp\left(-\frac{qV}{kT}\right)\right] \tag{7}$$

with $\rho_0 = qN_A$. Surface-state charges were not considered in this analysis. At the silicon surface, the equations appropriate to a dielectric interface were applied.

With this approximation to the charge density, there is no sharply defined depletion region edge. However, calculations have shown that for $V \geq 0.1$ V, the silicon is practically totally depleted while for $V \leq 0.001$ V, there is almost no depletion. In the computational method adopted, (7) is incorporated directly into the finite difference relaxation formulas, so that the potential value resulting from one relaxation cycle is used to determine the charge density at the point for the succeeding cycle. Thus the depletion charge distribution adjusts in step with the potential distribution as the solution proceeds, until eventually a self-consistent solution of (6) is obtained to within the desired degree of accuracy. This concept provides computational economy as compared with a possible alternative method involving a sequence

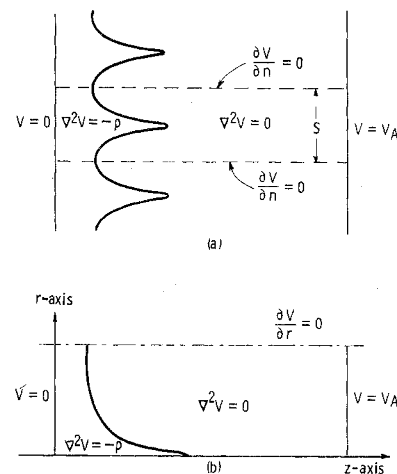

Fig. 2. (a) Basic-problem cell. (b) Reduced-problem cell used in the computer analysis.

of complete relaxation solutions each made with a fixed charge distribution while the charge distribution is modified in an outer loop.

After exploring several very simple approximations to the actual emitter geometry, the approximate shapes shown by the heavy lines in Fig. 3 were used. The structure is 10 μm high, tapering to a flat tip of 0.33-μm radius, and the separation between emitters is 20 μm. The model was set up on a finite difference net with 3 meshes per μm. The anode position and potential were arranged for an average field strength of 10^5 V/cm. The angular contour of the emitter is the result of limitations of the computer program to represent curved interfaces. For the semiconductor, $K_s = 12$ was used, while for the metallic emitter calculations, the potential on the surface of the emitter was held at zero, equivalent to no field penetration.

The lighter lines represent calculated equipotentials, and their shape for the metal, shown in Fig. 3(a), is as expected. For the p-semiconductor of 10 $\Omega\cdot$cm, there is significant field penetration, as seen in Fig. 3(b). Using the $V = 0.005$ V equipotential as the edge of the scr, the width of the scr is 1 μm in the "valley" between emitters, but considerably larger in the emitter under the tip. This is the result of the field enhancement. The equipotential lines and scr of a metallic and a p-semiconductor for a modified emitter structure are shown in Fig. 3(c) and (d), respectively. Here the tip was sharpened from a flat top to a 45° shape, where the triangular tip falls on the boundary of one mesh square. A significant increase of β from 9.6 to 18 is observed for the metallic point, while for the semiconductor, it increases from 5 to only 5.2.

Fig. 4 shows a more detailed comparison of the field intensification factor β for metallic and p-semiconducting field emitters (solid and open circles, respectively), as a function of the emitter height to tip radius ratio, h/r. The emitter shape of Figs. 3(c) and (d) was assumed. It is apparent that for metallic emitters, β increases with increasing h/r values, as expected, and the relationship $\beta = 1 + 0.36\ h/r$, was established empirically, assuming

Authorized licensed use limited to: IEEE Xplore. Downloaded on March 6, 2009 at 10:39 from IEEE Xplore. Restrictions apply.

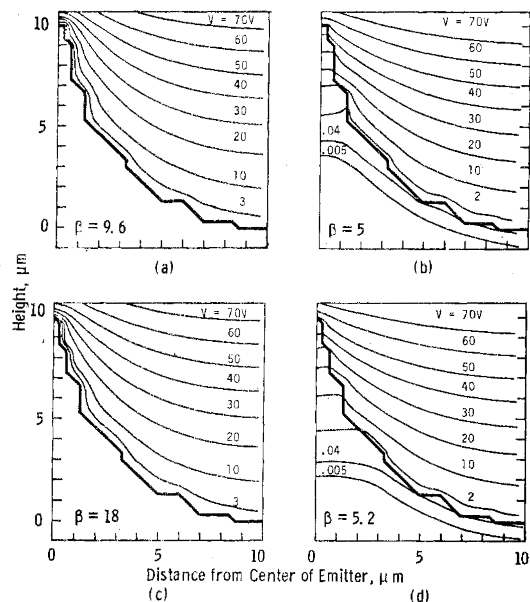

Fig. 3. Computer-calculated equipotential lines for (a) metallic, (b) p-silicon, (c) metallic, and (d) field-emitter structures. The field-intensification factor is given for each case.

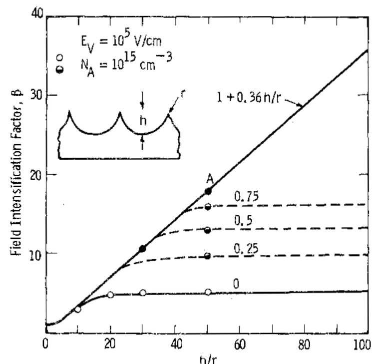

Fig. 4. Calculated field-intensification factor for metal (●) and p-silicon (○) in depletion and for various surface charges (◒). For metallic emitters the theoretical line $\beta = 1 + 0.36\ h/r$ is also shown.

that the emitters have a semicircular geometry as shown in the inset in Fig. 4. However, in the case of fully depleted p-type silicon emitters, β is generally very low (~ 5) and independent of the h/r ratio of the emitters. Thus in field emission from p-semiconductors, β depends not solely on the geometry of the emitter and the emitter spacing, but is profoundly influenced by the penetration of the field into the semiconductor in contrast to metallic emitters where there is no field penetration. This is an important result and some of its practical implications will now be discussed.

Experimentally, the h/r ratio of the silicon emitters was determined from high resolution SEM examinations to be in the range of 1000 ($h = 10\ \mu$m and $r \simeq 100$ Å). With average applied fields of 10^5 V/cm, tunneling fields of 3 to 4×10^7 V/cm would therefore be expected at the emitter tips provided that they exhibit a metal-like emission behavior, as it was tacitly assumed in the linear F–N region (region I in Fig. 1). If, however, full scr depletion conditions exist in the emitters (i.e., for operation in the source-limited region II), β is only 5 and the electric field at the emitter tip (5×10^5 V/cm) would be far too low for field emission to be observed. This strongly suggests, then, that the formation of a deeply depleted scr region within the emitter as shown in Figs. 3(b) and (d) does not occur. Instead, the semiconductor interior is shielded, presumably by the presense of charge (fixed or mobile electrons) on the surface of the emitter, and β is thereby increased to levels which permit the occurence of field emission.

The effect of surface charge on β was investigated by computer calculations as follows. The surface charge over the entire surface of a metallic-like emitter was determined for an h/r value of 50 and shown as point A on Fig. 4. This is the minimum charge required for the voltage at the surface to be zero. The applied field was then raised with the charge held constant and β was recalculated. For a doubling of the field, the 0.5 data point of Fig. 4 resulted. The assumption is that doubling the field for constant surface charge is equivalent to reducing the surface charge by a factor of 2 for constant field. Similarly, the 0.75 and 0.25 data points were obtained. What these points and extrapolated curves show, is that a surface charge does indeed increase β, and any value of β between that of the totally depleted and the metallic case is possible. In an actual case, there is possibly a redistribution of charge when the field is raised and our calculations are intended to show the semi-quantitative behavior of p-semiconductor emitters. The actual change of surface charge is a complicated function which depends on dark current, irradiance, surface states, and doping concentration.

In light of the β dependence on field penetration (hence on anode voltage) and surface charge, the following model for the operation of a p-semiconductor field emitter is proposed. In region I of Fig. 1, where p-silicon emitters are well-described by the F–N tunneling theory for metals, there are sufficient electrons for emission to be barrier limited. Thus the surface charge of mobile electrons is high and so is the field intensification. When the supply of electrons decreases (limited by thermal generation in region II), the surface charge diminishes and field penetration into the semiconductor takes place. This in turn causes β to drop.

The β lowering acts as a feedback mechanism. Electrons emitted from the surface-charge reservoir at the tip cause more field penetration, which in turn causes β to drop, thereby decreasing the barrier transparency and the tunneling probability. The electron emission decreases and a steady-state condition is established. It is quite likely that surface states influence the device behavior in addition to these effects. Some indications are discussed in Section V on surface states, but their behavior is not well understood at present.

In region III, avalanche breakdown creates a higher surface charge which leads to larger β, higher barrier transparency, and stronger emission. This continues until,

Authorized licensed use limited to: IEEE Xplore. Downloaded on March 6, 2009 at 10:39 from IEEE Xplore. Restrictions apply.

in region IV, the current is entirely limited by the tunneling barrier.

Another important aspect is that quite uniform emission has been achieved from large-area p-silicon field emission arrays, a consequence of the fact that variations in tip radius (or emitter height) have a negligible effect on β under depleted scr mode operation. Since, in practice, effective β's of 100 or higher are necessary for observable field emission, it seems likely that depletion is quite shallow and therefore, emission is probably insensitive to variations in emitter geometries over small ranges. Fortunately, such small-range variations are within the capabilities of the present fabrication processes. In contrast, very poor emission uniformity has been reported from various large-area metallic emitters [19]–[21].

The β dependence on field penetration also explains the fields in the semiconductor. In the F–N region, for β's of 100–500 and average applied fields around 10^5 V/cm, the tip fields are in the 1–5 $\times$ 10^7 V/cm range. The field in the silicon is 1/12 this value and lies in the 1–4 $\times$ 10^6 V/cm range. Such high fields can exist in a semiconductor only if there is a sufficient density of charge at the surface. For example, it is well known that electric fields in the semiconductor of metal-oxide-semiconductor devices reach values in the mid-10^6 V/cm range under sufficiently strong inversion or accumulation conditions. In the case of a field emitter operating in the F–N regime, there is a sufficient surface concentration of mobile electrons to terminate these high fields. If β were independent of the anode voltage, then as the current becomes limited by the supply function (scr formation), it is reasonable to assume that the surface electron concentration would tunnel into vacuum and the high fields would have to be absorbed in the depleted scr. However, fields in the mid-10^6 V/cm range cannot exist in a depleted scr without avalanche breakdown. Our model thus suggests that as the surface charge decreases (deviation from F–N operation), β drops and the semiconductor surface field decreases proportionately. In fact, β and surface charge adjust to a steady-state condition in region II which is sufficient for emission but not for breakdown. This self-limiting adjustment between β and surface charge cannot be explained if β is not allowed to vary.

IV. DARK CURRENT

In the operation of the photosensitive field emitter, a positive voltage is applied to the anode as shown in Fig. 5. This gives rise to various electric field strength components: E_1 are those field lines terminating on mobile electrons at the surface of the emitting tips, E_2 lines terminate on negatively charged surface states, and E_3 terminate on ionized acceptors. To satisfy Gauss's Law, it is obvious that unless there is a sufficiently high surface-state charge to shield the interior of the device entirely, there must be a depleted space-charge region of width W. The scr width varies as shown in Fig. 5, because the field at the emitters is significantly higher than in the "valleys" between emitters, a result of the geometric field enhancement as discussed in Section III.

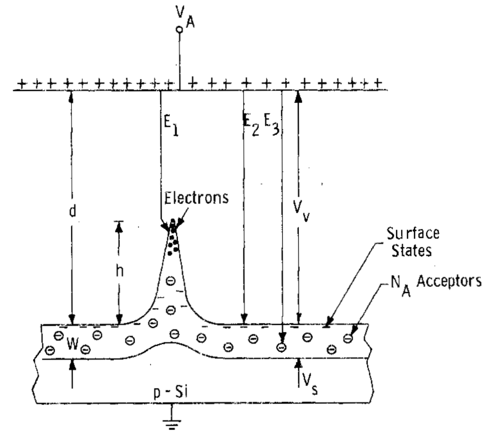

Fig. 5. Model of the field emitter used for dark-current calculations.

The dark current is considered to be due to thermally generated electron–hole (e–h) pairs in the scr, both in the bulk and at the surface. Since there can be a scr along the entire device, i.e., in the emitters and also between emitters, the volume in which bulk generation takes place is given by the width of the scr and the area of the entire array. Similarly, the area that determines surface generation is considered to be the entire area of the device, shown schematically in Fig. 5.

As shown in (2) and (3), the field at the emitter tip in vacuo is given by

$$E = \beta V_V/d \tag{8}$$

where β is voltage dependent. The field in the semiconductor, E_S, is diminished by the dielectric constant, K_S, and is also affected by any surface state charge Q_{SS}, as

$$E_S = E/K_S \pm Q_{SS}/K_S\epsilon_0 \tag{9}$$

where minus sign applies to negatively charged surface states while, for positive surface-state charge, the plus sign holds. E_S is related to the semiconductor bulk charge by Gauss's Law

$$E_S = qN_AW/K_S\epsilon_0. \tag{10}$$

Using (8), (9), and (10) in addition to the fact that the anode voltage, V_A, is the sum of the vacuum and semiconductor voltage drops, the scr width becomes

$$W = \epsilon_0 V_A/qN_Ad \pm N_{SS}/N_A \tag{11}$$

where N_{SS} is the density of surface states per unit area. The significance of the minus sign is that for negatively charged surface states, the field lines terminate partly on surface states, as depicted in Fig. 5. When the second term in (11) is equal to or larger than the first, it merely indicates that $W = 0$, since none of the field lines penetrate into the semiconductor and no space-charge region exists.

The scr width W of (11) is the width of the space-charge region in the planar region between emitters.

Authorized licensed use limited to: IEEE Xplore. Downloaded on March 6, 2009 at 10:39 from IEEE Xplore. Restrictions apply.

At the emitter itself, field intensification gives a higher field and W can be approximated by

$$W = \epsilon_0 \beta V_A / q N_A d \pm N_{SS}/N_A. \quad (12)$$

The dark current J_d is considered to be the result of thermal generation in the space-charge region bulk and surface and is given by [22]

$$J_d = q n_i W/\tau_g + q n_i s_0 \quad (13)$$

where τ_g and s_0 are the generation lifetime and surface-generation velocity, respectively [24]. Substitution of (12) in (13) gives

$$J_d = n_i \epsilon_0 \beta V_A/\tau_g N_A d \pm q n_i N_{SS}/\tau_g N_A + q n_i s_0. \quad (14)$$

A physical interpretation of (14) is as follows. The first term represents current generated in the space-charge region, which exists in the absence of surface states. The second term accounts for changes in W brought about by surface states. Clearly, the sum of these two terms must always be positive or zero. The third term is surface generation and applies as long as the surface is depleted. It should be pointed out that the current expression (14) is a first-order calculation. It was calculated for the plane-parallel case and then modified by the field-intensification factor of the emitters. Computer calculations, previously discussed, have shown that the field intensification factor depends on voltage when a scr exists in the emitter. The value of β adjusts itself to keep the field at the tip approximately constant.

The dark current considered previously is only thermally generated current. We have neglected the effect of the tunneling probability of these electrons. This is a good assumption, for our experiments have shown that electrons optically generated within the emitter array have a near unity probability of being emitted. We assume the same is true of thermally generated electrons. Another factor neglected in (14) is the electric field shielding by mobile electrons at the emitter, about which very little is known.

The most obvious test for the dark-current theory is its dependence on temperature. In (14), n_i is the most temperature-sensitive parameter. Emitter arrays were fabricated as described in [23]. For the dark-current measurements, areas of 0.5–1 cm² were etched, while for responsivity and modulation-transfer-function measurements, large area (5–7 cm²) arrays were fabricated. Experimental dark current–voltage curves are shown in Fig. 6. By plotting the current in the source-controlled region II as a function of inverse temperature in Fig. 7, straight lines are observed. The activation energy of 0.55 eV is approximately equal to $E_G/2$, i.e., it is the activation energy of n_i, confirming that generation of e–h pairs is determined by generation centers near midgap either in the bulk of the scr or at the surface.

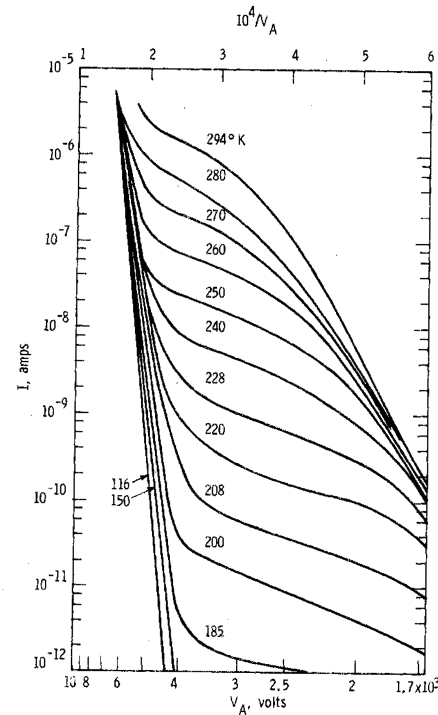

Fig. 6. The effect of temperature on the dark current of a 10 Ω·cm, p-type emitter array, unoxidized. $A = 0.5$ cm², $d = 3 \times 10^{-2}$ cm.

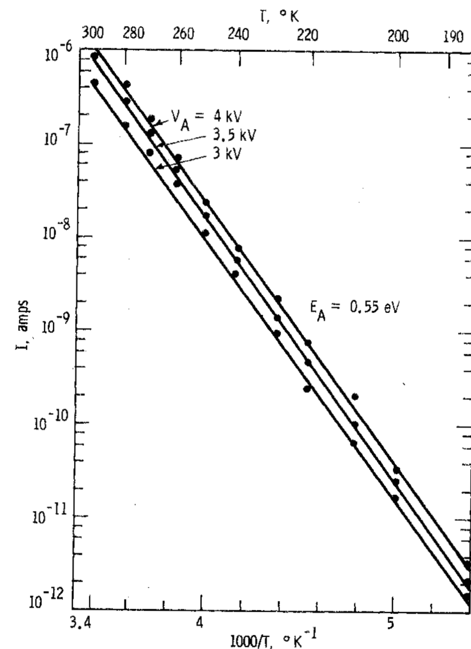

Fig. 7. Dark current as a function of temperature for the device of Fig. 6. The activation energy corresponds to $E_G/2$.

It is noted that the lowest current densities that have been measured are restricted to the 10^{-12} A/cm² range (at 180 K) due to spurious cold emission from supports etc. Extrapolation of the data of Fig. 7 suggests that current densities of 10^{-14} A/cm² should be obtainable at 150 K. However, such low dark levels may be unattainable in practice, since contributions from valence-band tunneling may become important at these low levels.

The dark current, according to (14), is inversely proportional to the bulk-dopant concentration, N_A.

Authorized licensed use limited to: IEEE Xplore. Downloaded on March 6, 2009 at 10:39 from IEEE Xplore. Restrictions apply.

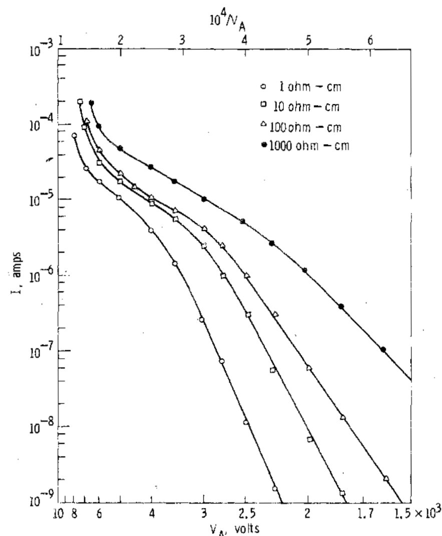

Fig. 8. The effect of resistivity on the dark current of p-type emitter arrays. $A \simeq 0.5$ cm², $d = 3 \times 10^{-2}$ cm.

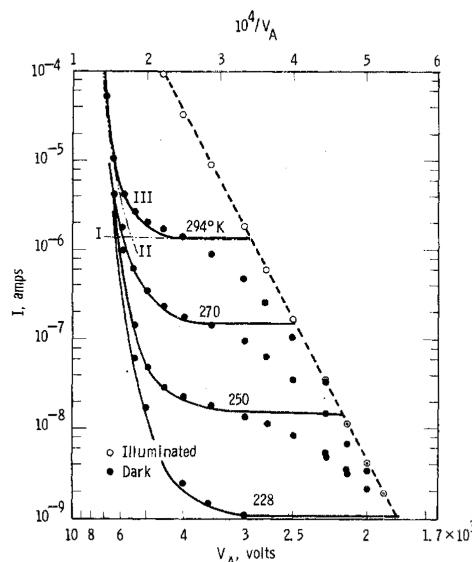

Fig. 9. Current as a function of voltage and temperature for the device of Fig. 6. Curves I, II, and III are discussed in the text and represent the dark-current model.

I–V characteristics of emitter arrays of resistivities varying between 1 and 1000 Ω·cm ($N_A = 2 \times 10^{16}$ to 1.3×10^{13} cm^{-3}) are shown in Fig. 8. It is apparent that the current decreases with increasing doping, but the inverse relationship between I and N_A is not strictly observed.

Bulk scr generation is characterized by the generation lifetime, τ_g, in (14). We investigated the effect of τ_g on the dark current by measuring the I–V characteristics of devices before and after phosphorus gettering. This was done using the $POCl_3$ technique [24] which is well proven for improving the lifetime in silicon devices [25]. The lifetimes were measured by the pulsed MOS (metal–oxide–semiconductor) capacitor technique [24] on test samples that underwent identical treatments as the emitter arrays. These measurements showed that $\tau_g \simeq$ 10–30 μs after thermal oxidation, which increased to 150–200 μs following the $POCl_3$ gettering step. However, no corresponding dark-current decrease could be observed indicating that such heat treatments, which are known to lower the dark current in conventional silicon p-n junction and MOS devices, do not seem to influence the dark current of emitter arrays. It appears, therefore, as if the surface current component is the dominant one.

In the derivation of (14), a number of parameters were used which are not well understood, nor can they be easily measured. For example, the density and type of surface states is not known; neither is the surface generation velocity. In view of these difficulties, and until more refined techniques are available for calculations and measurements of some of the parameters of (14), we use (13) for dark-current calculations. Here q and n_i are known and reasonable values for W, τ_g, and s_0 are available. For example, τ_g can be measured on test wafers that are exposed to heat treatments identical to those of the field emitter wafers.

The dark-current model is applied to the experimental curves of Fig. 6, as shown in Fig. 9. For an area of 0.5 cm², the dark-current expression is

$$I_d = 8 \times 10^{-20} n_i (W/\tau_g + s_0). \tag{15}$$

The lifetime τ_g was measured on test wafers to be 10 μs. For W varying between 1–30 μm (30 μm being the thickness of the wafer), the bulk-current component varies between 6.5×10^{-9} and 2×10^{-7} A at 294 K, lower than the experimental values. Furthermore, it was mentioned earlier that gettering, which improves the generation lifetime and hence should lower the bulk current component, had no effect on the dark current. This indicates that the surface current is the dominant component.

In order to match the experimental dark current to (15), s_0 was chosen to be 2000 cm/s to give

$$I_d = 1.6 \times 10^{-10} n_i. \tag{16}$$

This value for s_0 is reasonable for a silicon surface that has not been treated to reduce the fast surface state density, and according to [22] corresponds to a density around 10^{13} cm^{-2}.

Equation (16) is independent of voltage and merely indicates the thermally generated dark current, provided the surface is depleted. It is plotted in Fig. 9 as a function of temperature as line I. It matches the experimental dark current only over a restricted voltage range. By including an extrapolated breakdown current curve II, the sum III = I + II approaches the experimental data at high voltage. However, for lower voltages, there is some deviation. A possible explanation is that, in our model, the surface is assumed to be initially nondepleted and then depletes abruptly. In reality, the depletion region forms more gradually, starting at the tip where the field is highest and gradually depleting the entire area. The area is thus voltage dependent and the current gradually deviates from the F–N line.

Authorized licensed use limited to: IEEE Xplore. Downloaded on March 6, 2009 at 10:39 from IEEE Xplore. Restrictions apply.

In summary, the following model of dark current generation is proposed. At low anode voltages, the current follows the F–N dependence. For increasing voltage, the area around the tip depletes and the current is no longer limited by the barrier transparency, and the thermally generated electrons begin to dominate as the supply function. The depleted area increases gradually as a function of voltage and the dark current exhibits a similarly slow deviation from the F–N line. Eventually avalanche breakdown causes a rapid current increase. It appears that in the saturation-like region, the dark current is surfaced-generated current. This is in accord with our observations that treatments that influence bulk behavior (e.g., phosphorus gettering) have no effect on the dark current, while those that affect the surface behavior (e.g., H_2 annealing) have a very pronounced influence, as discussed in the next section. Obviously, surface states play a very important role in the operation of these devices. This has recently been confirmed by measurements of energy distributions of field-emitted electrons from p-silicon [26]. These data indicate emission from surface states energetically located between the Fermi level and the valence band. Our measurements of dark current also indicate emission from surface states, with the dominant emission from states near midgap as evidenced by the n_i-temperature dependence.

V. SURFACE STATES

Surface states have two entirely different effects on the operation of the device. They act as generation sites of e–h pairs when the surface is depleted. This effect is well known for p-n junctions and MOS devices [22]. In addition, they can either enhance or reduce the electric field in the silicon. This comes about as follows. Consider surface states that are neutral when occupied by holes. These states may have discrete levels in the energy gap or be continuously distributed. When the external field is applied to the field emitter, electrons are drawn to the surface where some are captured by the surface states, previously occupied by holes in p-type material, making them negatively charged. This allows them to act as field terminating charges (shown as E_2 in Fig. 5 shielding the interior of the device).

In spite of the fact that the internal field may be low as a result of surface-state shielding, the external field at the tip can be sufficiently high for field emission to occur. This implies that surface states may be helpful by shielding the semiconductor from high fields. However, they may also influence β in a manner similar to the effect of mobile electrons discussed earlier, i.e., raise β and hence the field. Which effect dominates would depend on the density and distribution of surface states.

Surface states have a further influence on the device behavior. By acting as capture sites for electrons, it is obvious that when the external field causes electrons to drift to the surface, enough of them are captured to fill the surface states. From Gauss's Law, the unit area charge in the semiconductor, N_S, depends on the field in the semiconductor as

$$E_S = qN_S/K_S\epsilon_0 = 1.5 \times 10^{-7} N_S \qquad (17)$$

for silicon. Except for the very tips of the emission array, where the field is highly intensified, the vacuum field is simply given by (3), i.e., $E_V = V_V/d \simeq 2 \times 10^5$ V/cm, which corresponds to $E_S \simeq 1.5 \times 10^4$ V/cm. From (17) this requires $N_S \simeq 10^{11}$ cm^{-2}. If the surface-state density $N_{SS} \geq N_S$, then all the electrons pulled towards the surface are captured by surface states. If, however, there are no surface states, then the surface electron charge required to satisfy (17) is held as an inversion layer, i.e., the electrons are mobile. The two cases of a device with and without surface states are illustrated schematically in Fig. 10.

The effect of this on the current–voltage behavior is shown in Fig. 11. A p-type array was fabricated and tested, resulting in the conventional curve (a) with fairly uniform emission over the emitting area. A 150-Å thick SiO_2 was then grown at 800°C in dry oxygen giving curve (b), which is very similar to (a), indicating that the presence of the thin SiO_2 layer does not appear to alter the surface barrier significantly. Annealing the device in hydrogen at 400°C for 1 h—a technique that results in a low surface-state density Si/SiO_2 interface for conventional oxidized Si devices—has a drastic effect on the current. The most pronounced change is the linearity of the I–V curve and the fact that it has become insensitive to light. A further experimental observation is a change in the emission pattern which is much less continuous and shows very spotty emission. After removing the oxide, the I–V curve returns to its original shape and the emission picture becomes more continuous. We propose the following mechanism. For curves (a), (b), and (d), there are surface states at the silicon surface. Electrons are captured and no inversion layer exists [Fig. 10(a)]. The dark current is due to thermal bulk and surface generation in the scr, and the electrons are emitted from the tips nearest where they are generated. After H_2 annealing, the surface-state density is greatly reduced and an inversion layer is formed. The entire array is now coupled via this layer and emission takes place mainly from the emitters with the highest field intensification. This is possible in this case since electrons can be supplied to these sites via the inversion layer. It is observed, in fact, that the current is higher even though the emission area has diminished and is more spotty. Further, if the current in (c) comes from emitters with higher field-intensification factors, then the slope of the log I–$1/V$ curve should be less than that of the other three curves. This is indeed the case as seen by comparing the F–N portions of the curves in Fig. 11. Photo-insensitive I–V curves were always observed whenever p-type emitter arrays were oxidized and subsequently annealed in hydrogen. However, when no deliberately grown oxide layer was present, the hydrogen anneal had no effect on the I–V characteristics. This is in

Authorized licensed use limited to: IEEE Xplore. Downloaded on March 6, 2009 at 10:39 from IEEE Xplore. Restrictions apply.

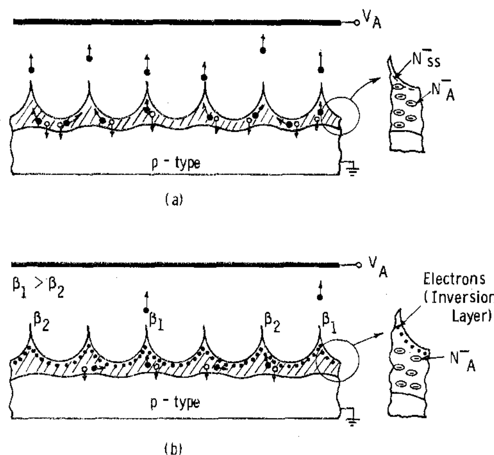

Fig. 10. Field-emitter schematic (a) with surface states capturing electrons and (b) without surface states allowing an inversion layer to form at the surface.

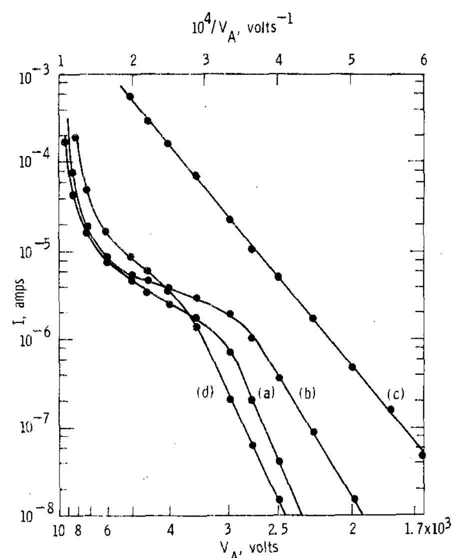

Fig. 11. Effect of oxide and hydrogen anneal on the dark current; (a) after etch, (b) 150 Å SiO_2, (c) 400°C 1 for H_2, (d) oxide removed. 10 Ω·cm p-Si, $A \simeq 0.3$ cm².

contrast to observations by Fursey *et al.*[1] who found that the nonlinearity of the I–V curves disappeared when the emitter was heated to 400–450°C in vacuo. Theirs was an irreversible effect attributed to the formation of a "conducting skin" along the emitter.

To verify the inversion-layer model, boron ions were implanted into arrays which had been oxidized to 150 Å. The ions were implanted at 50 keV at a dose of 10^{14} cm^{-2} into the oxide-passivated arrays. The depth of implantation was around 2500 Å giving a volume concentration of approximately 4×10^{18} boron atoms/cm³. After implantation, the devices were annealed in nitrogen at 800°C for 1 h to restore electrical activity and then in hydrogen at 400°C for 1 h. These arrays showed nonlinear I–V plots typical of p-arrays, indicating that the implanted p^+ layer appears to have decoupled the emitters from one another, by preventing the formation of an inversion layer.

VI. SPECTRAL RESPONSIVITY

It was stated earlier that the current in the source controlled region II of the I–V characteristics (Fig. 1) is very dependent upon the electron population in the conduction band and consequently on any stimulus that alters that population. One way of increasing the electron concentration is the absorption of photons of energy $h\nu \geq E_G$, generating e–h pairs, thus making the device a useful photoemitter with several unique properties. In contrast to conventional S-type photocathodes [27] and the more recent negative-electron affinity [28] devices—both of which require cesiation—the field emitter photocathode has no inherent long wavelength threshold, does not require cesiation (i.e., it is airstable), and furthermore does not need any high-field or high-temperature forming treatments. In addition, because of the moderately doped substrate (typically 10 Ω·cm), the electron diffusion length is quite long. For recombination lifetimes of 10 μs the diffusion length is approximately 150 μm. Hence photogenerated carriers have a very high internal quantum yield, since any electrons generated in the scr or within a diffusion length from the edge of the scr have a very high probability of being emitted. In fact, *internal* quantum efficiencies approaching unity have been measured.

The model for the *external* quantum yield calculations is shown in Fig. 12. Photons are incident on the field emitter, operating in the transmissive mode, from the left. The reflectivities R_0, R_1, and R_2 correspond to the air/pyrex, the pyrex/silicon, and the silicon/vacuum interfaces, respectively. While R_0 and R_1 cause some of the light to be reflected away from the silicon, R_2 is beneficial in that it allows some of the longer wavelength radiation, which has been transmitted without absorption, to be reflected back into the device for additional e–h pair generation. A further component, nonabsorbed radiation reflected from the aluminized phosphor screen, has not been considered here.

The field emitter is characterized by a neutral bulk of thickness t and diffusion length L, a depleted scr of width W, and a "dead" layer, δ, at the pyrex/silicon surface. The "dead" layer had to be invoked in order to obtain agreement between theory and experiment. The properties of the "dead" layer are well described by its name, i.e., the lifetime is considered to be so short that minority carriers generated within it are lost and hence cannot diffuse to the tips to contribute to the photocurrent. The origin of the "dead" layer is most likely the band bending of the silicon surface by the presence of the pyrex substrate, such that a sink for minority carriers is created. A "dead" layer is also introduced when a high–low junction is formed to reduce the surface recombination velocity, s, at the light-admitting side of the device [25],[29]. However, devices described here do not have such junctions and consequently s is quite high.

Authorized licensed use limited to: IEEE Xplore. Downloaded on March 6, 2009 at 10:39 from IEEE Xplore. Restrictions apply.

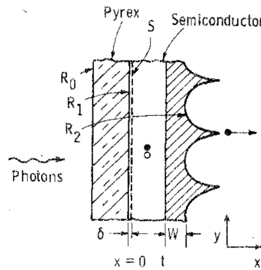

Fig. 12. Model used in the spectral-responsivity and modulation-transfer-function calculations.

Using the model of Fig. 12, the quantum yield is given by [30]

$$\eta_0 = \frac{\alpha LF}{(\alpha^2L^2-1)} \{m[1 + R_2 \exp(-2\alpha t)] + \alpha L[1 - R_2 \exp(-2\alpha t)] - \alpha L(1 - R_2)D \exp(-\alpha t) - (1 + R_2)(m \cosh\theta + \sinh\theta) \exp(-\alpha t)\}/D + F[1 - \exp(-\alpha W)] \exp(-\alpha t) \quad (18)$$

where

$$m = sL/D_n, \qquad \theta = t/L, \qquad D = m \sinh\theta + \cosh\theta$$

and

$$F = \frac{\exp(-\alpha\delta)(1 - R_0)(1 - R_1)}{[1 - R_0R_1 - (R_0R_2(1 - R_1)^2 + R_1R_2) \exp(-2\alpha t)]}. \quad (19)$$

Equation (18) differs from that in [30] in that absorption within the depleted scr of width W is taken into account by the last term in the equation. In the calculation, W is an average of the values applicable in the emitters and the "valleys" between emitters and the value of 5 μm was used.

Calculated yield curves are compared with experimental data in Fig. 13. The best fit with the transmissive-mode data are obtained with $s = 2 \times 10^4$ cm/s, $\delta = 0.8$ μm, and $L = 50$ μm. The absorption coefficients used in these calculations are those of Dash and Newman [31] at 77 K, since the data at 90 K [32], the temperature of measurement, are given only for wavelengths near 1 μm. The quantum-yield expression (18) represents the electrons generated within the device. The fact that there is quite good agreement between experiment and theory indicates that the escape probability of these electrons is very close to unity.

The devices were fabricated by electrostatically bonding [23] p-type substrates to pyrex faceplates. No shallow p^+ layer was formed on these devices necessitating the high values of surface recombination velocity in the calculations. The "dead" layer is possibly the result of band bending introduced by the bonding process, which causes minority carriers to be collected at the Si/pyrex interface with a correspondingly high s value. Surface recombination velocities of around 100 cm/s can be achieved with p^+/p high–low junctions [25], and theoretical curves (1) and (2) in Fig. 13 were computed with such s values and a reasonable value of minority carrier diffusion length as is obtainable with gettering. We expect that curve (2) is an upper limit to the quantum yield that can be expected for transparent silicon photo-field emitters at 77–90 K for a Si thickness of 30 μm.

In addition to transmissive data, experimental points are also shown for operation in the reflective mode. For the long wavelengths, the two sets of data are similar, but for $\lambda < 0.7$ μm, i.e., in the visible, the reflective yield is substantially higher, indicative of photon absorption at the electron-emitting side of the array. It is noted that for both transmission and reflection quantum-yield measurements, the aluminized phosphor screen was replaced by a transparent NESA glass anode in order to avoid errors due to light feedback from microscopic pinholes in the aluminized phosphor layer.

Quantum efficiency curves were also calculated for silicon devices operating at room temperature. These are shown in Fig. 14 for the same device parameters as were used in Fig. 13. The main difference from the 77 K curves is that as a result of high absorption coefficients, the quantum efficiency is lowered for short wavelength and increased for long wavelengths. This points out the importance of a thin "dead" layer. An experimental point of 7.5 percent at 1.06 μm is shown, which is the optimum that can be expected for a device 30 μm thick. Curve (2) was calculated with bulk and surface parameters routinely achievable and it shows that efficiencies of 70 percent at 0.9 μm, 7.5 percent at 1.06 μm, and 0.8 percent at 1.1 μm are possible at room temperature.

To complement the silicon quantum yields, we have calculated similar curves for germanium photosensitive field emitters, since it has been established that emission from germanium is feasible [2],[5]. These curves are shown in Fig. 15, where the curves, (1), (2), and (3) were derived using the surface and bulk recombination parameters and "dead" layer thicknesses corresponding to those of Fig. 13. The optical absorption coefficients were those of [31] for 77 K. These curves show that for reasonable values of s, L, and δ, efficiencies of 10–50 percent should be achievable to $\lambda = 1.45$ μm and imaging is possible to about 1.6 μm. The rather abrupt drop in η at 1.41 μm is due to the abrupt increase of α at that wavelength, corresponding to excitation of electrons from the valence band to the conduction band by direct transition.

Curve (2) in Fig. 13 shows that maximum yields of 40 percent at 0.86 μm and 28 percent at 0.9 μm are possible with the present silicon array structure when the device is operated near 77 K. The 1.06-μm yield at this temperature is around 0.2 percent, but values as high as 7.5 percent have been measured at room temperature. The currently attainable 1.06-μm quantum yields from thick (reflective) and thin (semi-transparent) silicon array structures are summarized on the absorption vs. target thickness plots shown in Fig. 16. It is evident that the 1.06-μm absorption within a given layer thickness decreases rapidly as the

Authorized licensed use limited to: IEEE Xplore. Downloaded on March 6, 2009 at 10:39 from IEEE Xplore. Restrictions apply.

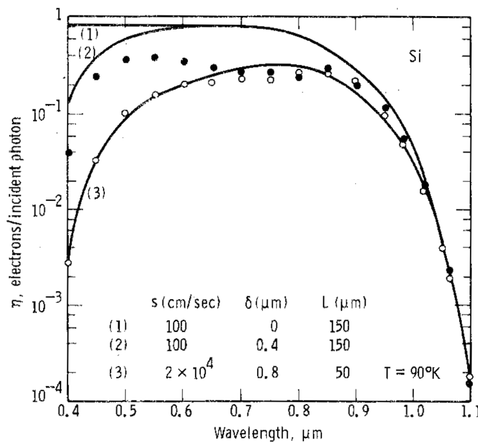

Fig. 13. Experimental (data points) and theoretical (lines) quantum efficiency curves. The parameters used in the calculations are shown on the figure. $V_A = 4$ kV, $t = 30$ μm, $W = 5$ μm, $A = 5$ cm^2.

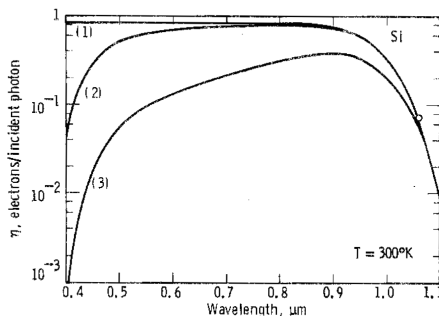

Fig. 14. Theoretical quantum efficiency curves for silicon field-emitter arrays operated at 300 K. The parameters used in the calculations of the three curves correspond to those of Fig. 13.

temperature is reduced. This imposes some limitations to the 1.06-μm performance of the semi-transparent structures which must, at present, be cooled to 90 K for low dark-current operation. The cause of the low yield at low temperatures is the increasing bandgap as the temperature is decreased with a corresponding smaller absorption coefficient.

The experimental quantum yield points on Fig. 16 agree fairly well with absorption curves with the exception of the 296 K "thick target" data point. The latter is plotted for the real target thickness of 250 μm. However, if the minority carrier diffusion length is less than this, then the effective thickness, which is just the diffusion length, should be used. On the 296 K, $\alpha = 16$ cm^{-1} line, the experimental value of $\eta = 15$ percent corresponds to a thickness of 100 μm, a reasonable value for the diffusion length of the device which was not gettered.

The "multiplication-mode" data correspond to yield measurements performed with the device biased at the onset of the avalanche breakdown region III in Fig. 1. Substantially higher photoelectric yields can be obtained in this mode of operation, as shown in Fig. 17. Curves (1) and (2) are experimental and (3) corresponds to curve (1) in Fig. 13. In fact, efficiencies above 100 percent have been measured by us for Si and have been previously

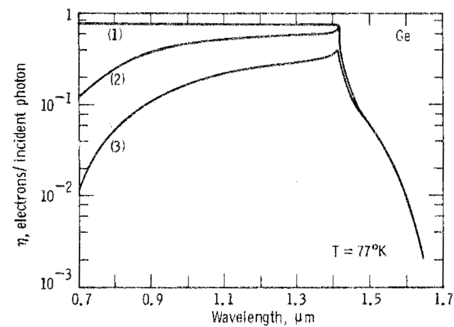

Fig. 15. Theoretical quantum-efficiency curves for germanium field-emitter arrays. The parameters used in the calculations of the three curves correspond to those of Fig. 13.

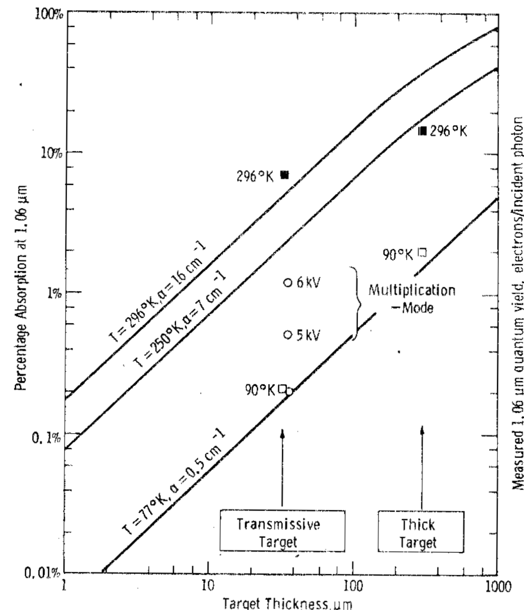

Fig. 16. Plots of the 1.06-μm absorption vs. thickness for silicon at various temperatures. Experimental data are 1.06-μm quantum yields of silicon field-emission arrays measured in reflection, □, and transmission, ○. Data were obtained at V_{anode} of 4 kV except where noted otherwise.

reported for Ge [5]. It should be noted, however, that while such multiplicative gains can be usefully employed to reduce the number of secondary gain stages in an intensifier device, the excess noise introduced by this multiplication process may deteriorate the operation of the photocathode under low light level imaging conditions. The emission uniformity, which might be expected to deteriorate when the device is operated in the multiplication mode, *actually improves* in this mode of operation. Since phosphor saturation effects are absent at the very low screen loading levels applicable here, this apparent self limiting behavior of field-emission arrays at high anode voltages is believed to be the result of field intensification factor adjustment as discussed previously.

VII. SPATIAL FREQUENCY RESPONSE

In the derivation of the quantum-yield expression, the incident radiation was laterally uniform. For the spatial frequency response analysis, the incident light was

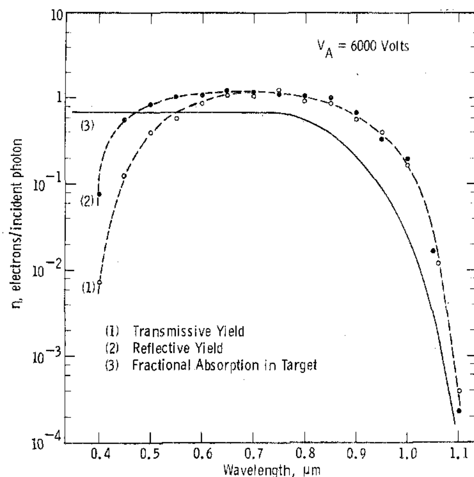

Fig. 17. Spectral response of point-array photoemitter (silicon (111), 10 Ω·cm, p-type, 30 μm thick) at 90 K and V_A = 6 kV (multiplication-model). Measurements made in transmission (curve 1) and reflection (curve 2). The calculated fractional absorption in target thickness is shown in curve 3.

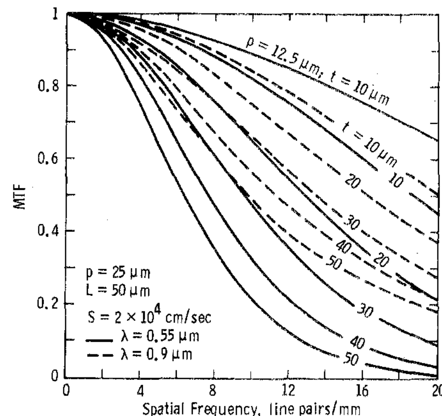

Fig. 18. Calculated MTF curves as a function of spatial frequency for the model of Fig. 12, considering lateral electron diffusion and the discrete nature of the emitter.

assumed to be stationary, monochromatic, and varying in intensity only in the transverse direction.

The spatial frequency response is conveniently represented by the modulation transfer function (MTF), which is the ratio of the output of the device when the input is sinusoidally modulated, to the output when the input has zero spatial frequency. It is given by [33]

$$\text{MTF}_i = \eta_k/\eta_0 \tag{20}$$

where η_0 is given by (18) and η_k is similar, except that the diffusion length L is replaced by an effective value L' [33]:

$$L' = L/(1 + k^2L^2)^{1/2}. \tag{21}$$

The quantity k is the radial frequency per unit distance given by $k = 2\pi N$, with N being the spatial frequency in line pairs per unit distance. For $N = 0$, i.e., uniform irradiation, the MTF_i value is unity.

The MTF_i is the modulation transfer function that results from lateral diffusion of minority carriers in the undepleted region of the emitter. The actual MTF of the device is degraded by the discrete nature of the field emitter, because emission occurs only at the emitter locations. This effect of discrete structures has been treated in great detail by Revuz [33]. The result is that the actual MTF can be written as

$$\text{MTF} = \text{MTF}_i \sin(\pi Np)/(\pi Np) \tag{22}$$

where the MTF_i term is determined by the carrier motion within the semiconductor and the $\sin x/x$ term is the result of the discrete structure. Equation (22) is valid for $N < 1/p$. Since $\sin x/x < 1$ for $x > 0$, it is clear that the discrete nature of the photoemitter reduces the MTF.

Calculated MTF curves are shown in Fig. 18. It is quite evident that the MTF depends quite strongly on the undepleted width t. The wider this region, the more lateral diffusion can take place before the minority carriers reach the scr. The other observation in Fig. 18 is that the wavelength can have a substantial influence on the MTF. The reason for this is that the shorter wavelengths are absorbed closer to the surface with a correspondingly longer distance to diffuse through. The dotted curves are for a wavelength of 0.9 μm corresponding to α = 110 cm^{-1}, while the solid lines are for λ = 0.55 μm with $\alpha = 3.7 \times 10^3$ cm^{-1}. The curves were calculated for L = 50 μm and $s = 2 \times 10^4$ cm/s, the values that were used in the spectral response calculations. It is interesting to note that the "dead" layer thickness has essentially no effect on the MTF. One further observation is that the values of L = 150 μm, s = 100 cm/s, and t = 30 μm, which were used as an upper limit in the efficiency calculations, gave a curve which coincided with the t = 50 μm curve of Fig. 18 for λ = 0.55 μm. This indicates that, while an improved diffusion length and surface recombination velocity is required for high quantum efficiencies, the spatial frequency response suffers because the carriers can diffuse over larger distances.

The MTF curves were calculated for emitter spacings of 25 μm except for the uppermost one which corresponds to a spacing of 12.5 μm. It shows that for a 10-μm thick device with 12.5-μm emitter-to-emitter spacing, the MTF at 20 line pairs/mm is expected to be 65 percent for the particular L and s values shown. These dimensions are probably near the limit for real emitter structures, and, for such a device, the limiting spatial frequency is 80 line pairs/mm at an MTF of 0.05.

In the correction term $\sin x/x$, which takes into account the discrete nature of the device, the spatial phase between the emitters and the light pattern was not considered. Such a phase shift can have a very significant influence on the MTF as shown in Fig. 19. Consider a spatial frequency such that $N = 1/2p$, i.e., one wavelength spans two emitter spacings as shown in Fig. 19(a). For zero phase difference, where the peaks and valleys of the modulated light signal coincide with the emitters, the $\sin(\pi Np)/(\pi Np)$ term becomes $2/\pi$. However, a 90° phase shift makes the response go to zero. Physically, this is shown in Fig. 19(b) where the 90° shift causes e–h pairs to be generated between emitters, resulting in

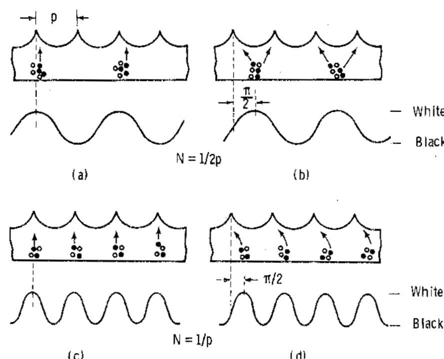

Fig. 19. Schematic representation of the effect of spatial phase shifts on the MTF.

diffusion to emitters on either side, thus smearing out the modulation. From Fig. 19(c) and (d) it is obvious that, for $N = 1/p$, the response is zero regardless of the phase, since there are carriers generated for each emitter. For $N \ll 1/p$ the phase is unimportant.

The theoretical response curves of Fig. 18 were calculated without taking the phase angle into consideration and therefore are the best possible MTF values. Any phase shift degrades the response with more severe effects towards the higher spatial frequencies. In the extreme of 90° phase shift, all MTF values at 20 line pairs/mm ($N = 1/2p$) are zero for $p = 25$ μm.

In addition to these MTF degradation mechanisms, there is a further degradation common to all proximity-focused image intensifiers. It is the result of the distribution in energy and direction of emergence of the photoelectrons from the photocathode. Emitted electrons with a lateral component of energy or direction are given a sideways acceleration by the applied field. A first-order discussion of this has been given for conventional photocathodes [34]. However, lacking definitive data of the energy distribution of the field-emitted electrons, it is presently not possible to estimate this effect quantitatively.

The only resolution measurements were carried out by projecting the image of a resolution chart on to the back of the photoemitter using a tungsten lamp as the illumination source. Tests were performed with white light and also by using filters to pass only wavelengths beyond 0.85 μm. The best limiting resolution measured was 10 line pairs/mm. Since this device was 35-μm thick, the curves of Fig. 18 show that the limiting resolution should have been higher. We expect that short-range nonuniformities in emission and degradation due to the proximity-focussed tube are the cause for the low measured value.

VIII. CONCLUSIONS

The dark-current effect of surface states, responsivity, and spatial frequency response of field-emission photocathodes has been analyzed both theoretically and experimentally. The devices were fabricated on silicon using an etch technique, and small-area ($0.5 - 1$ cm^2) devices were used for the dark-current studies while large-area ($5 - 7$ cm^2) devices were used for the responsivity and MTF measurements.

The field-emission photocathode is a new type of photoemitter, which exhibits some unique advantages. These are: (a) there is no inherent long wavelength emission threshold (the threshold is determined by the bandgap of the semiconductor) and (b) it has high quantum yields as a result of long minority-carrier diffusion lengths and high-escape probability. Using high resistivity p-Si, experimental transmissive mode photocathodes were developed with primary quantum yields of 25 percent at 0.86 μm and 7.5 percent at 1.06 μm. Calculations have shown that for Si operated at 77 and 300 K, the respective possible yields are 40 percent and 70 percent at 0.86 μm, 28 percent and 65 percent at 0.9 μm, and 0.3 percent and 7.5 percent at 1.06 μm. Since there is no long wavelength emission threshold, it is possible to use germanium for photoemission to 1.6 μm. Theory indicates that quantum yields of 40 percent to 1.4 μm and 1 percent at 1.6 μm are attainable. When field-emitter photocathodes are operated in the avalanche mode, photoelectric yields exceeding 100 percent have been achieved for both Si and Ge.

A present limitation of the silicon field-emitter photocathode is the room-temperature dark current of around 10^{-6} A/cm^2, which is predominantly the result of surface generation in the depleted space-charge region at the emitting surface. Devices thus far have been operated near 90 K with dark currents less than 10^{-12} A/cm^2. Such low temperatures result in low quantum yields at wavelengths near the bandgap energy because of inefficient photon absorption, when the bandgap widens with decreasing temperature.

The discrete nature of the photoemitter degrades the spatial frequency response. Nevertheless, modulation transfer function values of 40 percent at 15–20 line pairs/mm are shown to be possible with existing structures and for optimized geometries 65 percent at 20 line pairs/mm. These values will be somewhat degraded as a result of the inherent limitations of a proximity-focused device.

The field-emitter photocathode is a useful device where dark current and spatial frequency response are not of primary concern. Its main advantage lies in the high achievable quantum yields and the fact that it is the only device where efficient emission beyond 1.1-μm wavelength has been demonstrated. It is recommended that areas of future research include dark-current reduction and the development of large-area emitters for semiconductors of narrower energy gap than silicon.

ACKNOWLEDGMENT

The authors wish to thank R. A. Wickstrom and R. R. Papania for their excellent technical assistance and T. W. O'Keeffe for the preliminary computer study.

REFERENCES

[1] G. N. Fursey and N. V. Egorov, "Field emission from p-type Si," *Solid State Phys.*, vol. 32, pp. 23–29, Mar. 1969.

[2] J. R. Arthur, "Photosensitive field emission from p-type Ge," *J. Appl. Phys.*, vol. 36, pp. 3221–3227, Oct. 1965.

[3] O. H. Hughes and P. G. Bristow, "Field emission from GaP," *Solid State Phys.*, (a), vol. 2, pp. 503–509, July 16, 1970.
[4] I. L. Sokol'skaya and G. P. Shcherbakov, "Nonlinearity of the volt-ampere characteristics of field emission from CdS single crystals," *Sov. Solid State Phys.*, vol. 4, pp. 31–36, July 1962.
[5] P. G. Borzyak, A. F. Yatsenko, and L. S. Miroshnichenko, "Photo-field-emission from high resistance Si and Ge," *Solid State Phys.*, vol. 14, pp. 403–411, April 1, 1966.
[6] See for example, R. L. Bell and W. E. Spicer, "3–5 compound photocathodes: a new family of photoemitters with greatly improved performance," *Proc. IEEE*, vol. 58, pp. 1788–1802, Nov. 1970.
[7] V. F. Bibik, P. G. Borzyak, and A. F. Yatsenko, "Ge and Si field electron-emission photoelements," *Ukrainian Phys. J.*, vol. 13, pp. 621–622, Nov. 1968.
[8] R. S. Wagner and W. C. Ellis, "The vapor-liquid-solid mechanism of crystal growth and its application to Si," *Trans. Met. Soc. AIME*, vol. 253, pp. 1053–1064, June 1965.
[9] R. N. Thomas and H. C. Nathanson, "Photosensitive field emission from Si point arrays," *Appl. Phys. Lett.*, vol. 21, pp. 384–386, Oct. 15, 1972 and "Transmissive-mode silicon field emission array photoemitter," *Appl. Phys. Lett.*, vol. 21, pp. 387–389, Oct. 15, 1972.
[10] R. Gomer, *Field Emission and Field Ionization*. Cambridge, Mass.: Harvard University Press, 1961.
[11] R. E. Burgess, H. Kroemer, and J. M. Houston, "Corrected values of Fowler–Nordheim field emission functions v(y) and s(y)," *Phys. Rev.*, vol. 90, p. 515, May 15, 1953.
[12] G. Busch and T. Fischer, "Field emission from Si," *Phys. Cond. Matter*, vol. 1, pp. 367–393, 1963.
[13] A. F. Yatsenko, "On a model of photo-field emission from p-type semiconductors," *Solid State Phys.*, vol. 1, pp. 333–348, Feb. 16, 1970.
[14] L. M. Baskin, O. I. Lvov, and G. N. Fursey, "General features of field emission from semiconductors," *Solid State Phys.*, vol. 47, pp. 49–62, Sept. 1, 1971.
[15] P. G. Shlyakhtenko, R. Z. Bakhtizin and N. V. Mileshkina, "Connection between electrical breakdown and the form of the volt-ampere characteristics of the autoemission current from p-Ge," *Sov. Solid State Phys.*, vol. 14, pp. 1320–1322, Nov. 1972.
[16] H. Tomaschke and D. Alpert, "Field emission from a multiplicity of emitters on a broad-area cathode," *J. Appl. Phys.*, vol. 38, pp. 881–883, Feb. 1967.
[17] D. K. Schroder and R. N. Thomas, "Experimental confirmation of the Fowler–Nordheim law for large area field emitter arrays," *Appl. Phys. Lett.*, vol. 23, pp. 15–16, July 1, 1973.
[18] N. V. Egorov, G. N. Fursey, and S. P. Manokhin, "Generality of auto-electron emission from n-type and p-type semiconductors," *Sov. Solid State Phys.*, vol. 13, pp. 2612–2613, April 1972.
[19] H. E. Cline, "Multineedle field emission from the Ni-W eutectic," *J. Appl. Phys.*, vol. 41, pp. 76–81, Jan. 1970.
[20] H. Pfleiderer and H. Rehme, "Spike cathode for field emission," *Solid State Phys.*, vol. 11A, pp. 153–160, May 16, 1972.
[21] R. N. Thomas and B. J. Shaw, unpublished results on Cu-Cr eutectic alloy emitters.
[22] D. J. Fitzgerald and A. S. Grove, "Surface recombination in semiconductors," *Surf. Science*, vol. 9, pp. 347–369, Feb. 1968.
[23] R. N. Thomas, R. A. Wickstrom, D. K. Schroder, and H. C. Nathanson, "Fabrication and some applications of large-area silicon field emission arrays," *Solid-State Electron.*, vol. 17, pp. 155–163, Feb. 1974.
[24] D. K. Schroder and J. Guldberg, "Interpretation of surface and bulk effects using the pulsed MIS capacitor," *Solid-State Electron.*, vol. 14, pp. 1285–1297, Dec. 1971.
[25] T. M. Buck, H. C. Casey, J. V. Dalton, and M. Yamin, "Influence of bulk and surface properties on image sensing silicon diode arrays," *Bell Syst. Techn. J.*, vol. 47, pp. 1827–1854, Nov. 1968.
[26] B. F. Lewis and T. E. Fischer, "Energy distributions of field-emitted electrons from silicon: evidence for surface states," *Surf. Sci.*, vol. 41, pp. 371–376, Feb. 1974.
[27] A. H. Sommer, *Photoemissive Materials*. New York: Wiley, 1968.
[28] B. F. Williams and J. J. Tietjen, "Current status of negative electron affinity devices," *Proc. IEEE*, vol. 59, pp. 1489–1497, Oct. 1971.
[29] D. K. Schroder, J. Guldberg, D. Green, H. C. Nathanson, and R. A. Wickstrom, "Influence of the n^+ layer on the gain of electron-excited silicon diode array targets," *J. Appl. Phys.*, vol. 41, pp. 5038–5040, Nov. 1970.
[30] G. A. Allen, "The performance of negative electron affinity photocathodes," *J. Phys. D: Appl. Phys.*, vol. 4, pp. 308–317, Feb. 1971.
[31] W. C. Dash and R. Newman, "Intrinsic optical absorption in single-crystal germanium and silicon at 77 K and 300 K," *Phys. Rev.*, vol. 99, pp. 1151–1155, Aug. 15, 1955.
[32] G. G. MacFarlane, T. P. McLean, J. E. Quarrington, and V. Roberts, "Fine structure in the absorption-edge spectrum of Si," *Phys. Rev.*, vol. 3, pp. 1245–1254, Sept. 1, 1958.
[33] J. Revuz, "Contrast variation in junction mosaic targets," *Acta Electr.*, vol. 10, pp. 195–214, 1966; M. H. Crowell and E. F. Labuda, "The silicon diode array camera tube," *Bell Syst. Tech. J.*, vol. 48, pp. 1481–1528, May/June 1969.
[34] M. J. Needham and R. F. Thumwood, "A proximity-focussed image tube," *Advances in Electronics and Electron Physics*, vol. 28A, pp. 129–136, 1969.